ACS APPLIED MATERIALS & INTERFACES

RESEARCH ARTICLE

www.acsami.org

Controlled Synthesis of Vertically Aligned Hematite on Conducting Substrate for Photoelectrochemical Cells: Nanorods versus Nanotubes

Aiming Mao,[†] Kahee Shin,[†] Jung Kyu Kim,[†] Dong Hwan Wang,[‡] Gui Young Han,[†] and Jong Hyeok Park*[,†]

[†]Department of Chemical Engineering, Sungkyunkwan University, Suwon 440-746, Republic of Korea

[‡]Department of Chemical and Biomolecular Engineering, Korea Advanced Institute of Science and Technology (BK 21 Graduate Program), 373-1 Guseong-dong, Yuseong-gu, Daejeon 305-701, Republic of Korea

Supporting Information

ABSTRACT: This paper describes two different processes to synthesize vertically aligned hematite nanorod and nanotube arrays, respectively, on a conductive substrate by the electrochemical deposition method with the help of an anodized aluminum oxide nanotemplate. The two types of nanostructured hematite were used as the photoanode for photoelectrochemical cells. The hematite nanotubes exhibited much higher photoelectrochemical activity than the hematite nanorods, including an improved photocurrent density, more negative onset potential, better photon harvesting, and better charge carrier transfer ability. The observed behavior may offer new information to enhance the photocatalytic ability of hematite, which is considered to be one of the best photoanode materials in the research field of photoelectrochemical cells.

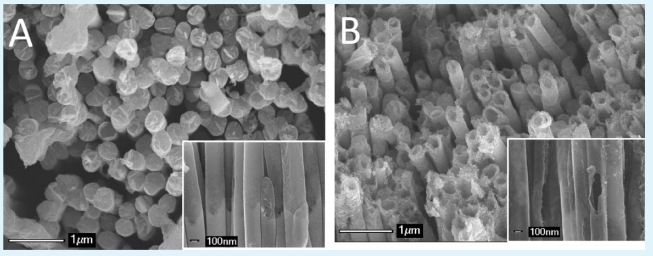

KEYWORDS: hematite, hydrogen, nanotube, water splitting

INTRODUCTION

The growing environmental concerns and increasing demand for energy have motivated the search for green, sustainable energy sources. The 120 000 terawatts (TWs) of solar radiation reaching the surface of the earth at any given time is expected to make a great contribution as a clean energy source. The direct use of solar energy through such technique as solar cells and solar thermal power is still limited, because they only work in daytime. Therefore, energy storage devices have to be employed to store the solar energy and use it during the night time. Hydrogen (H2) is considered to be one of the prime candidates as a future energy carrier. The photoelectrochemical generation of hydrogen by the photoelectrolysis of water is one of the most promising methods of utilizing and storing solar energy. Since the first report of hydrogen production using TiO_2 as a photoanode to decompose water under ultraviolet light illumination in 1972, much effort has been made to develop this technology.[1,2]

Of the materials being developed for photocatalytic applications, titanium dioxide (TiO_2) is considered the most promising because of its low cost, chemical stability, and photostability.[3,4] However, this catalyst functions under ultraviolet light, which accounts for only 4% of the incoming solar energy and thus renders the overall process impractical. Theoretically, to produce hydrogen from water, the conduction band edge of the semiconductor should be more negative than the reduction potential of H^+/H_2 (0 V vs NHE at pH 0), whereas the valence band edge must be more positive than the oxidation potential of O_2/H_2O (1.23 V vs NHE at pH 0). However, the semiconductor bandgap required to obtain a reasonable reaction rate should be larger than 2.03 eV (corresponding to a wavelength of 610 nm), because of the inevitable thermodynamic losses and kinetic losses.[5,6] Hence, *n*-type hematite (α-Fe_2O_3) has received considerable attention, because of its suitable bandgap of about 2.0−2.2 eV, which allows for the absorption of about 40% of the incident solar light. Moreover, the hematite has good photochemical stability (stable at pH > 3).[7] However, the range of applications of α-Fe_2O_3 in PEC cells is limited, due to the high electron−hole pair recombination rate resulting from its poor electrical conductivity and short hole diffusion length (less than 20 nm).[8] In addition, an external potential bias is necessary to drive the hydrogen generation, because conduction band edge of the hematite is slightly more positive than that of H^+/H_2 reaction.

To reduce the possibility of recombination, the doping of various metal ion species including Ti^{4+}, Ca^{2+}, Mg^{2+}, Cu^{2+}, Zn^{2+}, Rh^{3+}, Cr^{3+}, Sm^{3+}, Y^{3+}, Si^{4+}, Ge^{4+}, Pt^{4+}, V^{5+}, Nb^{5+}, and Mo^{6+} or surface electro-catalysts such as Pt, Au, and RuO_2 have been introduced.[9−24] The methods of doping were various, such as codeposition, sol−gel method and spray pyrolysis, and so on. After implantation of metal ions which acted as traps of

Received: November 30, 2010
Accepted: May 10, 2011
Published: May 10, 2011

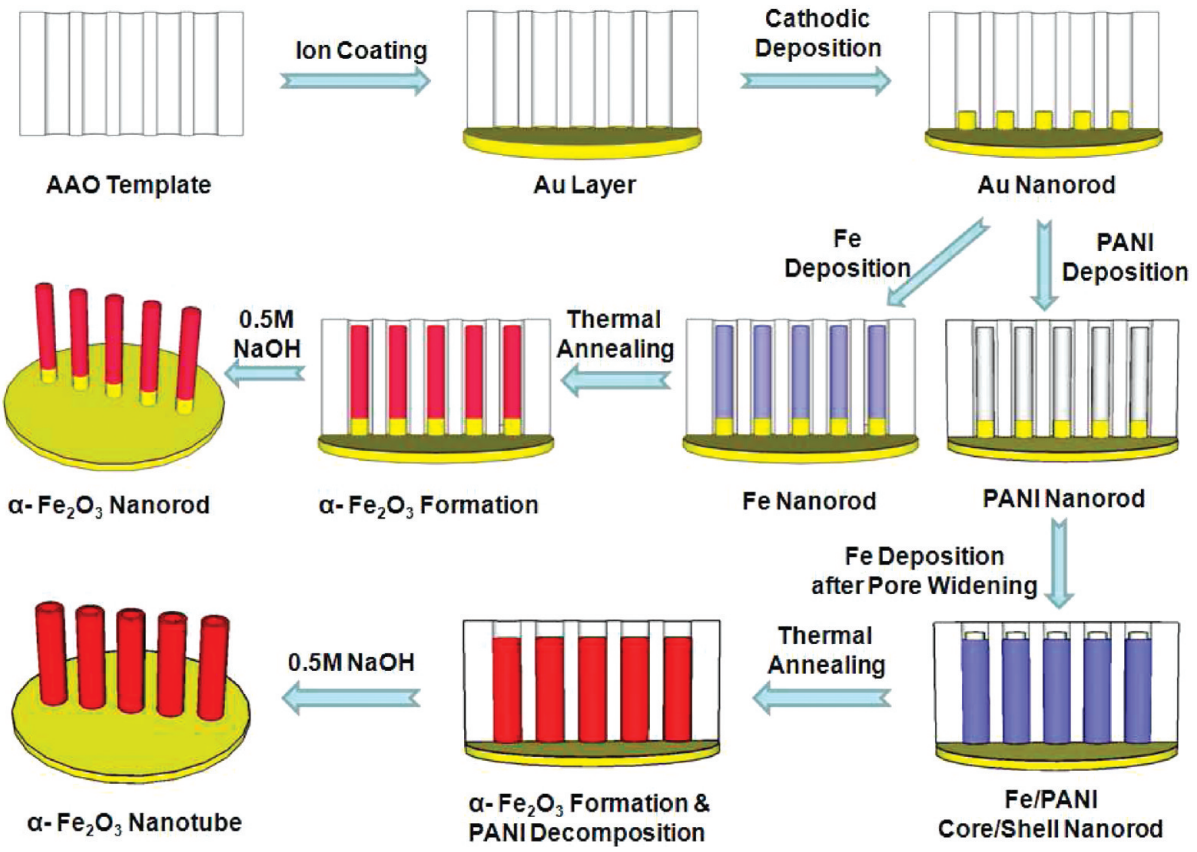

Figure 1. Schematic diagram of synthesis of α-Fe_2O_3 nanorods and α-Fe_2O_3 nanotubes on Au substrate.

photoexcited charge carriers into semiconductor lattice, significant variations in the electronic properties could be achieved, including, for example, the higher electrical conductivity, the lower activation energy, and the higher charge carrier density.[9,23] Noble metals, including Au and Pt, have lower Fermi levels than semiconductors. So, photoexcited electrons can be easily transferred from semiconductors to the metals, resulting in a lower possibility of recombination.[24−28] Thus, they are excellent catalyst for hydrogen evolution reaction. Oppositely, the RuO_2 is an excellent catalyst for oxygen evolution reaction.[9,29,30] The second approach to increase the photocatalytic activity of hematite involves the use of several nanostructured hematites. Generally, the poor hole transport is one of the main factors that limit the photoresponse of hematite based photoanodes. In addition, it is mostly accepted that the interfacial effects play a significant role in charge transport. Because the electrical conductivity of α-Fe_2O_3 is highly anisotropic,[31] charge transport is hindered at the interfaces between the crystallites with different orientations. Therefore, in contrast to nanoparticle film, one-dimensional (1D) nanostructures such as nanowires, nanotubes, and nanorods, with larger surface area and high aspect ratio, could improve the transportation of charge carriers and thus reduce the recombination losses at gain boundaries (see the Supporting Information, Figure S1). Moreover, the smaller diameter of hematite nanowires, nanorods or nanotubes, can minimize the distance for holes to diffuse to electrolyte-semiconductor interface, avoiding the poor charge transport limitation.[32−36] The idealized morphology for an hematite photoanode for water splitting was proposed to be 1D nanostructures vertilcally grown on a conducting substrate.[30,37] Lindiquist and co-workers first reported the use of hematite nanorod arrays as photoanodes in a PEC cell and demonstrated that 1D nanostructures could potentially address some of the fundamental PEC issues and increase the device efficiency.[14,15] The detailed comparsion of nanofilm and 1D nanostructures for water splitting application was report by Warren group, in which the better photoresponse was obtained by 1D nanostructured hematite photoanode.[38]

In this paper, two different vertically aligned nanostructures of α-Fe_2O_3 were synthesized on an Au substrate by the electrochemical deposition method. We introduce a method of synthesizing vertically aligned hematite nanotube and nanorod arrays. Figure 1 shows schematic diagram of the synthesis procedures for the nanorods and nanotubes. Then, we fabricated PEC cells and carefully investigated their photocurrent density in an aqueous electrolyte. This is the first report focusing on the comparison of vertically aligned α-Fe_2O_3 nanorods and α-Fe_2O_3 nanotubes in PEC cell applications.

EXPERIMENTAL SECTION

Materials and Chemicals. Template: Anodized Aluminum Oxide (AAO) (disk structure, with total diameter of 13 mm, an average pore-diameter of 200 nm and thickness of 60 μm, Whatman International Ltd.) Chemicals for Au electrodeposition: potassium gold cyanide ($KAu(CN)_2$, 99.99%, Alfa Asear) and potassium dihydrogen phosphate (KH_2PO_4, 99.0%, KANTO CHEMICAL CO. INC.). Chemicals for Fe electrodeposition: ferrous sulfate ($FeSO_4 \cdot 7H_2O$, 98.0%, Junsei Chemical Co. Ltd.), ascorbic acid ($C_6H_8O_6$, 99%, Sigma Aldrich), amidosulfonic acid (H_2NSO_3H, 99.99%, Sigma Aldrich) and boric acid (H_3BO_3,

99.99%, Sigma Aldrich). Chemicals for polyaniline electrodeposition: aniline (C_6H_7N, 99.5%, Sigma Aldrich), sulfuric acid (H_2SO_4, 95.0%, SAM CHUN PURE CHEMICAL Co. Ltd.)

Au Ion Coating on AAO. A thin layer of Au was sputtered onto (HOYEON Tech. Co. Ltd., sputtering current: 12 mA, sputtering time: 15 min) one side of an AAO template.

Synthesis of Au Nanorods (NRs) in AAO. The electrodeposition was carried out using an aqueous solution consisted of a 40 g L^{-1} $KAu(CN)_2$ and 100 g L^{-1} KH_2PO_4.[39] The Au nanorods were electrodeposited into the AAO pores in a traditional three-electrode system (see Supporting Information Figure S2). A Pt plate (1 cm ×5 cm) worked as the counter electrode and Ag/AgCl electrode (0.222 V vs SHE) acted as the reference electrode. The AAO template worked as the working electrode. The AAO template was pressed by an O-ring to creat tight contact between the Au sputtered bottom surface and a conductive Al thin foil with 15 mm diameter and 20 μm thickness. The Al plate was used only for connecting the AAO template with our potentiostate equipment. The opposite side (with open pore) was exposed to the electrolyte (area: ~1.0 cm^2). The Au nanorods were grown at a constant potential of −1 V for 5 min. The AAO with sputtered Au nanolayers and ~500 nm Au nanorods inside provided good electric conductivity for the electrodeposition of the target materials.

Synthesis of α-Fe_2O_3 Nanorods (NRs). After preparing the AAO template with Au layer, Fe nanorods were grown electrochemically into its pores from a solution containing Fe ions (60 g of ferrous sulfate, 1.5 g of ascorbic acid ($C_6H_8O_6$), 0.5 g of amidosulfonic acid (H_2NSO_3H), and 15 g of boric acid (H_3BO_3) in 1 L of distilled water), at a constant potential of −1.5 V vs Ag/AgCl.[40] The samples were then thermal annealed in an air atmosphere at 500 °C for 6 h to convert the Fe into crystalline α-Fe_2O_3. Finally, the AAO templates were removed by immersing the samples in 1 M NaOH solution.

Synthesis of α-Fe_2O_3 Nanotubes (NTs). Conducting polyaniline (PANI) nanorods (NRs) were electrodeposited into the pores of the AAO templates first by potentiostat cycling between 1.2 V to −0.2 V vs Ag/AgCl at a scan rate of 0.1 V/s, from an acid solution (0.1 M aniline, 0.5 M H_2SO_4 in water).[41] The length of the PANI NRs was controlled by adjusting the number of cycles. After the electrodeposition of the PANI NRs, the samples were dried at 80 °C in air to remove the solvent. The volume of the PANI NRs were shrinked during the drying process so that there was some space between PANI NRs and AAO pores. Then, the samples were further treated by immersing them into 0.5 M NaOH solution for 5 min to widen the generated space. Fe was then electrodeposited into the empty spaces between the shrunken PANI NRs and the walls of the AAO pores. The decomposition of the PANI NRs can occur during the thermal annealing step. The removal of the PANI NRs and the conversion of Fe into α-Fe_2O_3 can occur simultaneously. Finally, α-Fe_2O_3 nanotubes were obtained after the removal of the AAO template by immersing the samples in 1 M NaOH solution.

Characterization. The morphologies of the samples were obtained by scanning electron microscopy (FESEM, JSM-7000F, Japan). XRD measurements were carried out with a Siemens diffractometer D500/5000 in Bragg-Bretano geometry under Cu Ka radiation. High Resolution Transimission Electron Microscopy (HRTEM, JEM3010) studied were operated at an accelerating voltage of 300 eV. The samples were prepared by first dispersing the samples into ethanol through ultrasonic treatment and then dropping the dispersion on a carbon coated copper grid and drying the samples in air for observation. The photocurrent−voltage ($J-V$) behaviors were measured in a three-electrode configuration with 1 M NaOH as electrolyte, Ag/AgCl as reference, and a Pt plate as counter electrode. The potential of photoelectrode was controlled by a potentiosat (CH Instruments, CHI 660) and the scan rate was 20 mV/s. The samples with area 0.5 cm^2 were illuminated under a 150 W xenon lamp based solar simulator using a AM 1.5G filter (PECCELL, Yokohama, Japan, PEC-L01), whose light intensity was calibrated using a silicon reference cell (Fraunhofer ISE, Certificate No. C-ISE269). The measured light irradiance was AM 1.5G sunlight of 100 mW cm^{-2}. Incident photon-to-current efficiency (IPCE) measurement was carried out using a 300 W xenon light source and a monochromator (Polaronix K3100 IPCE Measurement System, McScience). Electrochemical impedance spectrocopy (EIS) was done in the same cell used in IPCE measurment by potentistat under AM 1.5G light illumination from solar simulator, in which the frequency scans from 100 000 to 0.025 Hz.

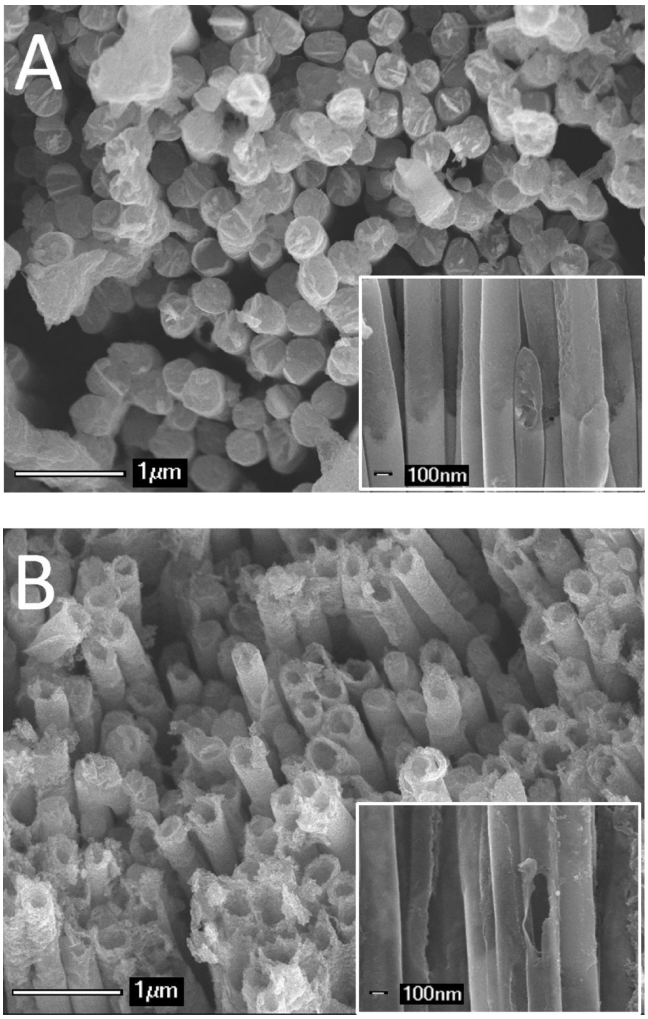

Figure 2. FESEM images: (A) α-Fe_2O_3 nanorods; (B) α-Fe_2O_3 nanotubes.

RESULTS AND DISCUSSION

The scanning electron microscopy images shown in panels A and B in Figure 2 show the α-Fe_2O_3 nanorod arrays and nanotube arrays, respectively. As can be seen from Figure 2A, the α-Fe_2O_3 nanorods with an average diameter of around 200 nm are well-defined. The cross-section view of the nanorods is shown in the inset of Figure 2A. The α-Fe_2O_3 nanorods grow vertically with a smooth surface. The uniform α-Fe_2O_3 nanotubes are shown in Figure 2B. The wall thickness of the tubes is about 40 nm. To prepare the vertically aligned α-Fe_2O_3 nanotubes, PANI nanorods are grown first and act as a template to generate the nanotube structure. As can be seen in Figure 2B, all of the nanotube arrays have an open pore structure and no PANI remained, because of the high temperature annealing condition

used to convert Fe into hematite. The inset SEM image in Figure 2B shows the cross-section view of the α-Fe_2O_3 nanotubes at a high magnification. As shown in this figure, the nanotubes are also well aligned with a high surface area. The observation of the broken part of one of the nanotubes further confirms that the α-Fe_2O_3 nanotubes are uniform and well-defined with a much higher surface area than that of the α-Fe_2O_3 nanorods (see the Supporting Information). In this study, the electrochemically deposited Fe was converted to crystalline α-Fe_2O_3 by the thermal annealing process. X-ray Diffraction (XRD) measurements were also performed to confirm the crystal structure of the samples. As you can see in Figure 3, the sharp and clear peaks of α-Fe_2O_3 nanorods and nanotubes perfectly match well with the reported peak positions (JCPDS No.24−0072). Images A and B in Figure 4 show the low magnification of TEM images of α-Fe_2O_3 nanorods and nanotubes, respectively. They confirm that hematite nanorods and nanotubes with uniform shape and a diameter about 200 nm were synthesized, in a good agreement with the SEM observation. The high-resolution TEM (HRTEM) images of nanorods and nanotubes are shown in images C and D in Figure 4, respectively. Both of them display regular lattice fringes with a spacing of 0.25 nm, corresponding to the (110) lattice plane of hematite, which clearly demonstrate that the nanorods and nanotubes have the same crystalline nanostructures.

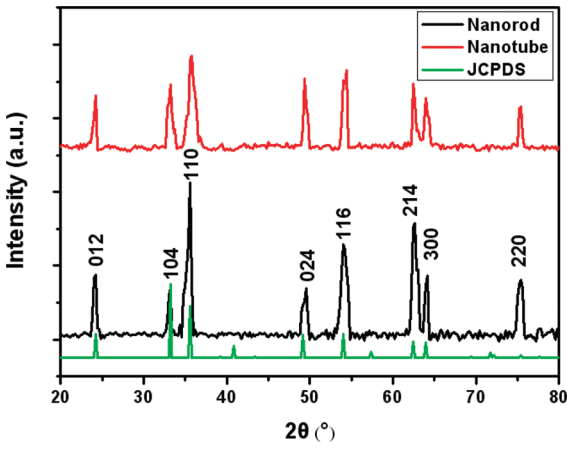

Figure 3. X-ray diffraction pattern of α-Fe_2O_3 nanorods and α-Fe_2O_3 nanotubes, compared with JCPDS 24−0072.

To investigate the photocatalytic activity of the α-Fe_2O_3 nanorods and nanotubes, their photocurrent−voltage ($J-V$) and electrochemical impedance were measured. The $J-V$ behavior is considered as an indirect way to measure the rate of hydrogen generation by water splitting if we assume the faradaic efficiency for water oxidation is unity.[9] In our study, the $J-V$ responses were measured under AM 1.5G simulated solar light irradiation in 1 M NaOH electrolyte. For the investigation of the effects of the nanostructures on the photoelectrochemical generation of hydrogen, a PEC cell was set up to measure the $J-V$ characteristics using the α-Fe_2O_3 nanorods or α-Fe_2O_3 nanotubes as the photoanode electrode. A Pt plate and Ag/AgCl electrode were used as the counter and reference electrodes, respectively. The $J-V$ curves of the α-Fe_2O_3 nanorods and α-Fe_2O_3 nanotubes are presented in panels A and B in Figure 5, respectively. In addition, the dependency of the photocatalytic activity of the tubes or rods on their length is investigated. With increasing length of the nanorods, the amount of photoexcited

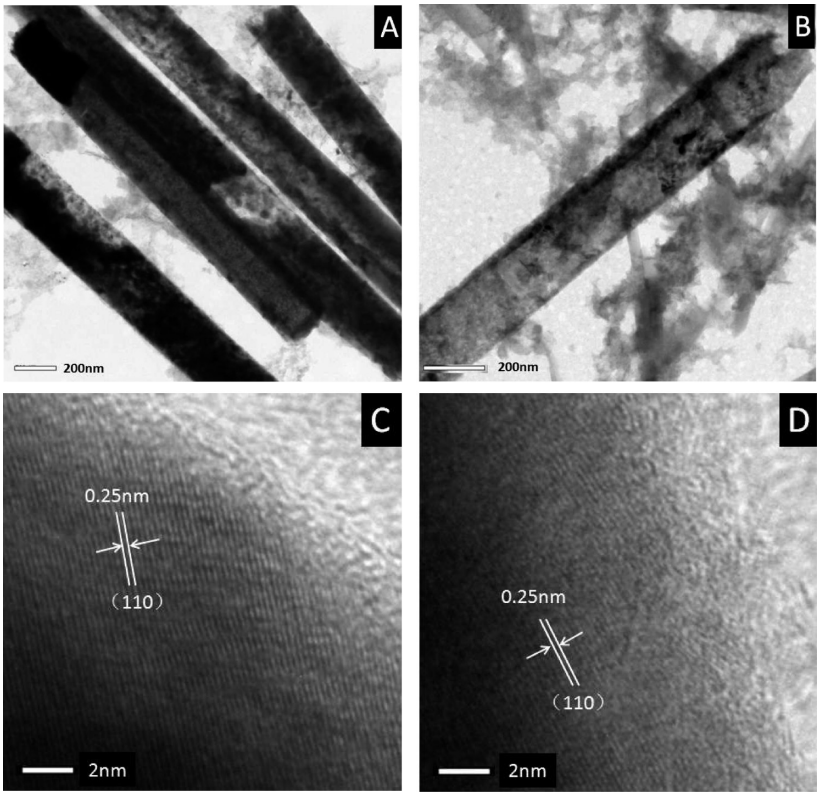

Figure 4. TEM and HRTEM images: (A) TEM of α-Fe_2O_3 nanorods; (B) TEM of α-Fe_2O_3 nanotubes; (C) HRTEM of α-Fe_2O_3 nanorods; (D) HRTEM of α-Fe_2O_3 nanotubes.

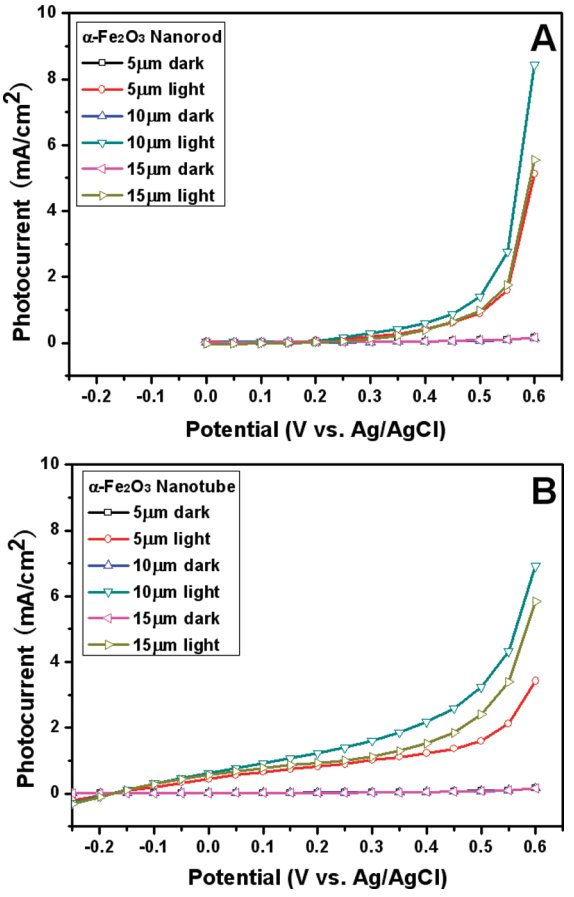

Figure 5. Photocurrent−voltage behaviors of (A) α-Fe_2O_3 nanorods and (B) α-Fe_2O_3 nanotubes under illumination by AM 1.5G light in 1 M NaOH electrolyte.

electron−hole pairs increases, thus increasing the photocurrent density. However, the recombination of the carrier pairs also increases with increasing length of the vertically aligned hematite, resulting in a decrease of the photocurrent density.[42] Therefore, it would be expected that there is an optimum length of the photoanode. From panels A and B in Figure 5, the best performance is obtained from the α-Fe_2O_3 nanorod and nanotube samples with a height of about 10 μm. From the Figure 5A, the onset potential of α-Fe_2O_3 nanorods around 0.2 V agrees well with the typical values reported in previous studies.[24,43−45] Figure 5B shows the $J-V$ responses of the α-Fe_2O_3 nanotubes. Compared to that of the nanorods, the onset potential of the nanotubes is shifted negatively to around −0.17 V because of the effective hole scavenging, which liberates more electrons making anode potential more electronegative.[44,46,47] In the low applied potential range, the photocurrent densities of the hematite nanotube arrays are higher than those of the nanorod arrays, indicating that the α-Fe_2O_3 nanotubes can increase the number of holes and electrons participating in the electrochemical reaction leading to the production of oxygen and hydrogen at the photoanode and counter electrode, respectively. In other words, the generated electrons should be transported through the hematite lattice to the current collector (Au layer) without recombining with the holes at the same external bias potential. In the case of the nanorod photoanode, when the diameter of the rods exceeds some critical point (the hole diffusion length), the

Table 1. Photocurrent Density Values (mA/cm^2) of Hematite Nanorods and Nanotubes at 0.43 V vs Ag/AgCl under AM 1.5G Light Illumination

	length (μm)		
structure	5	10	15
nanorod	0.42	0.59	0.38
nanotube	1.23	2.18	1.52

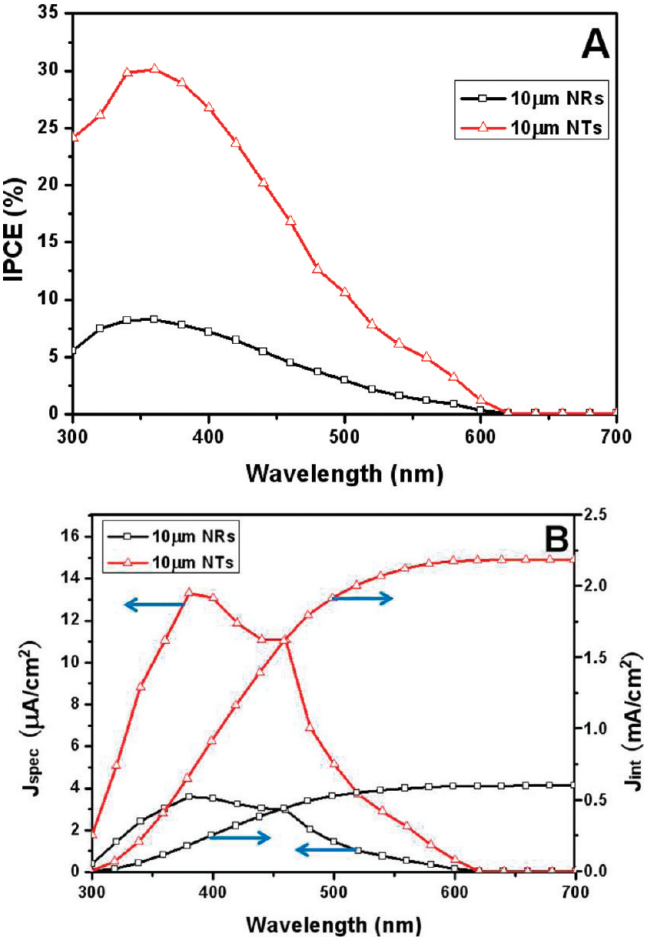

Figure 6. Spectral photoresponse of 10 μm long α-Fe_2O_3 nanorods and α-Fe_2O_3 nanotubes at 0.43 V vs Ag/AgCl under illumination by AM 1.5G light in 1 M NaOH electrolyte: (A) incident photon to current conversion efficiency (IPCE); (B) solar photocurrent spectral (J_{spect}) and integrated solar photocurrent (J_{int}).

recombination possibility of the photogenerated electrons and holes increases. The increase of the recombination rate decreases the photocurrent. On the other hand, in the case of the nanotube system, as the tube length increases, more photons of light are absorbed and, consequently, the photocurrent increases, as in the nanorod based PEC cell. However, irrespective of the tube length, the recombination rate of the photogenerated carriers might be always much lower than those of the nanorod based PEC cell, because of the large effective surface area in close proximity with the electrolyte, thus enabling the diffusive transport photogenerated holes to oxidize the species in the electrolyte. In the state-of-the-art hematite photoanode performance,

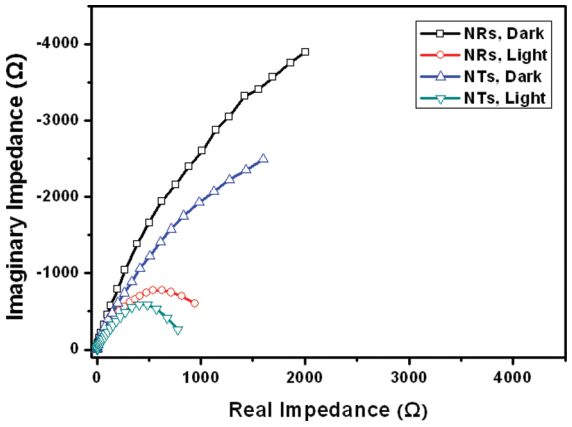

Figure 7. Electrochemical impedance behaviors of α-Fe_2O_3 nanorods and α-Fe_2O_3 nanotubes at 0.4 V vs Ag/AgCl under illumination by AM 1.5G light in 1 M NaOH electrolyte.

the photocurrent density is around 3.5 mA/cm^2 at 0.43 V vs Ag/AgCl.[48] In this study, the highest photocurrent density about 2.2 mA/cm^2 at 0.43 V vs Ag/AgCl was observed from 10 μm long nanotube based cell and the detailed photocurrent density values of nanorods and nanotubes are showed in the Table 1. However, higher photocurrent densities are observed in the nanorod based PEC cells in the high applied potential range. One possible reason for this is the difference in the total amount of active material that can absorb photon energy from the sun. The total amount of photoexcited electron and hole pairs generated by the α-Fe_2O_3 nanorods is more than that generated by the α-Fe_2O_3 nanotubes. At a high external potential, the generated electrons and holes can participate in electrochemical reaction with a lower probability of their recombining with holes.

The incident photon to current conversion efficiency (IPCE) was also measured in the same three-electrode system in 1 M NaOH electrolyte. Figure 6A shows the IPCE of 10 μm long nanorod and nanotube arrays measured at 0.43 V vs Ag/AgCl. Two samples show a maximum value between 340 to 380 nm, while the photoresponse drops gradually to zero at about 620 nm. As can be seen in Figure 6A, the nanotube arrays show much higher IPCE values than those of the nanorod arrays. It confirms that the nanotubes have better photon harvesting than nanorods at 0.43 V vs Ag/AgCl bias, which is consistent to the $J-V$ results shown in Figure 5. Multiplication of the IPCE with the photon flux density of AM 1.5G yields the solar photocurrent spectrum. And the total photocurrent can be obtained by integration over the spectrum (Figure 6B). As can be seen in Figure 6B, the integrated photocurrents of samples are very similar to the measured photocurrents from $J-V$.

Figure 7 shows the electrochemical impedance plots of the α-Fe_2O_3 nanorods and α-Fe_2O_3 nanotubes, respectively. All of the samples were tested in 1 M NaOH solution under AM 1.5G light illumination and 0.4 V bias. And the frequency range was from 100,000 to 0.025 Hz. As can be seen in Figure 7, the impedance spectrum is strongly affected by the light illumination. Both of the semicircles of hematite PEC became smaller under illumination conditions, suggesting that the photoexcited charge carriers decrease their charge transfer resistance.[44,49] In addition, the semicircle of nanotube sample is relative smaller than that of nanorod sample. It is fair to say that the charge transfer resistance is lower in the nanotube sample.

CONCLUSIONS

In summary, vertically grown α-Fe_2O_3 nanorod and nanotube arrays with a high aspect ratio were successfully synthesized by the template assisted electrochemical deposition method. Using this simple method, the two different nanostructures of the samples could be controlled more easily and precisely. Comparison studies of the α-Fe_2O_3 nanorod and nanotube arrays were conducted by performing photocurrent−voltage, incident photon to current conversion efficiency, and electrochemical impedance measurements. An enhanced photocurrent, negative shift of the onset potential, and better photoresponse spectrum were observed from the α-Fe_2O_3 nanotubes as compared to the α-Fe_2O_3 nanorods. In addition, the better charge transfer characteristics of the α-Fe_2O_3 nanotubes were confirmed by the electrochemical impedance measurements. These results show that the morphology control of nanostructures is important for the efficient fabrication of PEC cells from hematite. We believe that the information obtained in this study might help to increase the photocurrent density within hematite-based PEC cells.

ASSOCIATED CONTENT

Supporting Information. Schematic of the electron transport within different nanostructures (Figure S1) and schematic of three-electrode system for electrochemical deposition (Figure S2), and the calculated surface area of nanorod and nanotube. This material is available free of charge via the Internet at http://pubs.acs.org.

AUTHOR INFORMATION

Corresponding Author
*E-mail: lutts@skku.edu.

ACKNOWLEDGMENT

This research was supported by Future-based Technology Development Program (Nano Fields, 2010-0029321) and Research Programs (No. 20100026281, NRF-2009-C1AAA001-2009-0094157) through the National Research Foundation of Korea (NRF) funded by the Ministry of Education, Science and Technology (MEST). J. H. Park acknowledges the Seoul 'R&D Program'.

REFERENCES

(1) Fujishima, A.; Honda, K. *Nature* **1972**, *238*, 37–38.
(2) Boddy, P. J. *J. Electrochem. Soc.* **1968**, *115*, 199–203.
(3) Hadjiivanov, K. I.; Klissurski, D. K. *Chem. Soc. Rev.* **1996**, *25*, 61–69.
(4) Heller, A. *Acc. Chem. Res.* **1995**, *28*, 503–508.
(5) Weber, M. F.; Dignam, M. J. *J. Electrochem. Soc.* **1984**, *131*, 1258–1265.
(6) Bolton, J. R.; Strickler, S. J.; Connolly, J. S. *Nature* **1985**, *316*, 495–500.
(7) Ohmori, T.; Takahashi, H.; Mametsuka, H.; Suzuki, E. *Phys. Chem. Chem. Phys.* **2000**, *2*, 3519–3522.
(8) Dare-Edwards, M. P.; Goodenough, J. B.; Hamnett, A.; Ravellick, P. R. *J. Chem. Soc., Faraday Trans. I* **1983**, *79*, 2027–2031.
(9) Hu, Y. S.; Kleiman-Shwarsctein, A.; Forman, A. J.; Hazen, D.; Park, J. N.; McFarland, E. W. *Chem. Mater.* **2008**, *20*, 3803–3805.
(10) Watanabe, A.; Kozuka, H. *J. Phys. Chem. B* **2003**, *107*, 12713–12720.
(11) Bjorksten, U.; Moser, J.; Gratzel, M. *Chem. Mater.* **1994**, *6*, 858–863.

(12) Duret, A.; Gratzel, M. *J. Phys. Chem. B* **2005**, *109*, 17184–17191.
(13) Kay, A.; Cesar, I.; Gratzel, M. *J. Am. Chem. Soc.* **2006**, *128*, 15714–15721.
(14) Beermann, N.; Vayssieres, L.; Lindquist, S. E.; Hagfeldt, A. *J. Electrochem. Soc.* **2000**, *147*, 2456–2461.
(15) Lindgren, T.; Wang, H. L.; Beermann, N.; Vayssieres, L.; Hagfeldt, A.; Lindquist, S. E. *Sol. Energy Mater. Sol. Cells* **2002**, *71*, 231–243.
(16) Hu, Y. S.; Kleiman-Shwarsctein, A.; Forman, A. J.; Stucky, G. D.; McFarland, E. W. *J. Phys. Chem. C* **2008**, *112*, 15900–15907.
(17) Ingler, W. B.; Khan, S. U. M. *Int. J. Hydrogen Energy* **2005**, *30*, 821–827.
(18) Mohanty, S.; Ghose, J. *J. Phys. Chem. Solids* **1992**, *53*, 81–91.
(19) Leygraf, C.; Hendewerk, M.; Somarjai, G. A. *J. Catal.* **1982**, *78*, 341–351.
(20) Gurunathan, K.; Maruthamuthu, P. *Int. J. Hydrogen Energy* **1995**, *20*, 287–295.
(21) Radwan, N. R. E. *Appl. Catal., A* **2004**, *273*, 21–33.
(22) Kumari, S.; Singh, A. P.; Sonal, D. D.; Shrivastav, R.; Dass, S.; Satsangi, V. R. *Int. J. Hydrogen Energy* **2010**, *35*, 3985–3990.
(23) Glasscock, J. A.; Barnes, P. R. F.; Plumb, I. C.; Savvides, N. *J. Phys. Chem. C* **2007**, *111*, 16477–16488.
(24) Mao, A.; Park, N. G.; Han, G. Y.; Park, J. H. *Nanotechnology* **2011**, *22*, 175703.
(25) Sakthivel, S.; Shankar, M. V.; Palanichamy, M.; Arabindoo, B.; Bahnemann, D. W.; Murugesan, V. *Water Res.* **2004**, *38*, 3001–3009.
(26) Li, F. B.; Li, X. Z. *Chemosphere* **2002**, *48*, 1103–1111.
(27) Kim, S.; Choi, W. *J. Phys. Chem. B* **2002**, *106*, 13311–13317.
(28) Subramanian, V.; Wolf, E. E.; Kamat, P. *J. Am. Chem. Soc.* **2004**, *126*, 4943–4950.
(29) Rajeshwar, K. *J. Appl. Electochem.* **2007**, *37*, 765–787.
(30) van de Krol, R.; Liang, Y. Q.; Schoonman, J. *J. Mater. Chem.* **2008**, *18*, 2311–2320.
(31) Iordanova, N.; Dupuis, M.; Rosso, K. M. *J. Chem. Phys.* **2005**, *122*, 144305.
(32) Fellenz, N. A.; Bengoa, J. F.; Marchetti, S. G.; Sives, F. R.; Stewart, S. J.; Mercader, R. C. *Hyperfine Interact.* **2006**, *170*, 75–82.
(33) Abid, M.; Abid, J. P.; Jannin, S.; Serrano-Guisan, S.; Palaci, I.; Ansermet, J. P. *J. Phys.: Condens. Matter* **2006**, *18*, 6085–6093.
(34) Zhao, L. Y.; Eldridge, K. R.; Sukhija, K.; Jalili, H.; Heinig, N. F.; Leung, K. T. *Appl. Phys. Lett.* **2006**, *88*, 033111.
(35) Tang, Y.; Chen, Q. *Chem. Lett.* **2007**, *36*, 840–841.
(36) Zhong, Z.; Ho, J.; Teo, J.; Shen, S.; Gedanken, A. *Chem. Mater.* **2007**, *19*, 4776–4782.
(37) Li, Y.; Zhang, J. Z. *Laser Photon. Rev.* **2009**, *4*, 517–528.
(38) Khan, S. U. M.; Sultana, T. *Sol. Energy Mater. Sol. Cells* **2003**, *76*, 211–221.
(39) Wu, B.; Boland, J. J. *J. Colloid Interface Sci.* **2006**, *303*, 611–616.
(40) Mohapatra, S. K.; Banerjee, S.; Misra, M. *Nanotechnology* **2008**, *19*, 315601.
(41) Shin, T. Y.; Yoo, S. H.; Park, S. H. *Chem. Mater.* **2008**, *20*, 5682–2686.
(42) Bi, D.; Wu, F.; Yue, W.; Guo, Y.; Shen, W.; Peng, R.; Wu, H.; Wang, X.; Wang, M. *J. Phys. Chem. C* **2010**, *114*, 13846–13852.
(43) Mao, A.; Han, G. Y.; Park, J. H. *J. Mater. Chem.* **2010**, *20*, 2247–2250.
(44) Rangaraju, R. R.; Panday, A.; Raja, K. S.; Misra, M. *J. Phys. D: Appl. Phys.* **2009**, *42*, 135303.
(45) Kleiman-Shwarsctein, A.; Hu, Y. S.; Forman, A. J.; Stucky, G. D.; McFarland, E. W. *J. Phys. Chem. C* **2008**, *112*, 15900–15907.
(46) Mohapatra, S. K.; John, S. E.; Banerjee, S.; Misra, M. *Chem. Mater.* **2009**, *21*, 3048–3055.
(47) Rangaraju, R. R.; Raja, K. S.; Misra, M. *Electrochim. Acta* **2010**, *55*, 785–793.
(48) David Tilley, S.; Cornus, M.; Sivula, K.; Gratzel, M. *Angew. Chem., Int. Ed. Engl.* **2010**, *49*, 6405–6408.
(49) Lopes, T.; Andrade, L.; Ribeiro, H. A.; Mendes, A. *Int. J. Hydrogen Energy* **2010**, *35*, 11601–11608.